Research Article

Journal of Environmental Nanotechnology

Green Synthesis, Structural Characterization and Kinetics of Photocatalytic Degradation of Reactive Blue 19 Dye Using CeO_2-doped Reduced Graphene Oxide Nanohybrid

A. Loganathan[1*], N. Sethupathi[2], P. Mahalingam[3] and P. Sivakumar[3]

[1]Department of Chemistry, Thiruvalluvar Government Arts College (Affiliated to Periyar University, Salem), Rasipuram, TN, India
[2]Department of Physics, Arignar Anna Government Arts College (Affiliated to Periyar University, Salem), Namakkal, TN, India
[3]Department of Chemistry, Government Arts and Science College (Affiliated to Periyar University, Salem), Komarapalayam, TN, India
Received: 18.02.2026 Accepted: 01.03.2026 Published: 30.03.2026
*loghunadan@gmail.com

ABSTRACT

The development of visible-light-active photocatalysts through sustainable synthetic routes remains a critical challenge in wastewater remediation. In this study, a CeO_2-doped reduced graphene oxide (CeO_2/rGO) nanohybrid was synthesized using *Carica papaya* leaf extract as a green reducing agent. The resulting catalyst exhibited a surface area of 95 m^2/g, a narrowed optical band gap of 2.91 eV, and uniformly distributed CeO_2 nanoparticles with an average size of 4–8 nm as confirmed by HRTEM. Structural and spectroscopic analyses validated the formation of a stable CeO_2/rGO hybrid with enhanced charge separation efficiency. The photocatalytic activity was evaluated through the degradation of Reactive Blue 19 (RB19) under UV and solar irradiation. Nonlinear regression using a fractional-order Langmuir–Hinshelwood kinetic model achieved superior fitting accuracy over conventional linearized models, with reaction orders ranging from 0.30–0.58 under varying irradiation conditions. Notably, this approach provides enhanced insight into non-ideal surface reaction behavior, highlighting its advantage over commonly applied integer-order kinetic analyses. The nanohybrid retained more than 95% degradation efficiency after four successive cycles, demonstrating excellent stability. These results indicate that green-synthesized CeO_2/rGO is a promising, sustainable photocatalyst for treatment of dye-laden wastewater.

Keywords: CeO_2/rGO; Green synthesis; Fractional-order kinetics; Langmuir–Hinshelwood; Reactive Blue-19; Photocatalysis.

1 INTRODUCTION

The contamination of water bodies by synthetic dyes from textile industries has become a critical environmental challenge across developing nations. Reactive dyes, particularly anthraquinone- and azo-based structures such as Reactive Blue 19 (RB19), exhibit high thermal and chemical stability, strong chromophoric character, and resistance to biodegradation. As a consequence, even trace quantities of such dyes disrupt aquatic ecological balance, reduce light penetration, hinder photosynthesis, and may generate toxic or mutagenic intermediates. Conventional physicochemical treatment processes, including adsorption, coagulation–flocculation, membrane filtration, and advanced oxidation, often suffer from limitations such as incomplete mineralization, high sludge generation, elevated operational costs, and restricted reusability of materials (Wu *et al.* 2025). Therefore, the development of efficient, stable, and environmentally benign catalysts for complete dye degradation remains an urgent scientific priority (Kumar *et al.* 2025). Semiconductor-based photocatalysis has emerged as an effective and sustainable pathway for degrading organic pollutants under UV or solar light. Metal oxides such as TiO_2, ZnO, CeO_2, and WO_3 are widely investigated due to their redox versatility and photochemical stability (El Mchaouri *et al.* 2025). However, many of these materials suffer from key drawbacks including a wide band gap, fast electron–hole recombination, poor visible-light utilization, and limited surface active sites. To address these issues, hybrid photocatalysts that integrate metal oxides with carbonaceous nanomaterials have gained significant interest (Ansari *et al.* 2025; Sahu *et al.* 2024). Reduced graphene oxide (rGO) is particularly attractive due to its exceptional electrical conductivity, high specific surface area, π-conjugated structure, and ability to facilitate rapid charge carrier migration (Mondal *et al.* 2021). Coupling metal oxides with rGO has been shown to enhance light absorption, suppress recombination, and provide additional adsorption sites for pollutant molecules.

Cerium oxide is a promising photocatalyst owing to its unique Ce^{4+}/Ce^{3+} redox pair, oxygen storage capacity, and defect-rich lattice. When integrated with rGO, CeO_2 nanoparticles benefit from improved electron

transport, enhanced surface reactivity, and better dispersion (Ahamed *et al.* 2025). However, the controlled synthesis of CeO_2/rGO hybrids remains challenging, particularly when using environmentally hazardous reducing agents such as hydrazine. Green synthesis approaches using plant extracts have recently attracted attention as they offer biocompatible, non-toxic, and cost-effective alternatives for producing nanomaterials (Villagrán *et al.* 2024). Plant-derived biomolecules can act simultaneously as reducing, stabilizing, and capping agents, enabling sustainable pathways toward composite formation.

Photocatalytic degradation processes are inherently complex, involving multiple steps such as photon absorption, charge carrier generation, surface adsorption of reactants, and subsequent redox reactions. These processes are strongly influenced by surface heterogeneity, active site distribution, and intermediate species formation. As a result, the overall reaction kinetics often deviate from ideal linear or pseudo-first-order behaviour typically assumed in conventional analyses. Therefore, to better capture these complexities, nonlinear and fractional-order kinetic approaches become essential for accurately describing the photocatalytic reaction mechanism. Nonlinear Langmuir–Hinshelwood (LH) models, particularly fractional-order kinetic approaches, offer improved accuracy in describing actual photocatalytic processes (Wang, 2018). However, such nonlinear kinetic analyses are rarely applied to CeO_2/rGO photocatalytic systems.

The present work investigates a green synthetic strategy for preparing CeO_2/rGO using *Carica papaya* leaf extract as a natural reducing agent. The structural, optical, and morphological features of the nanohybrid are systematically analyzed, with particular emphasis on CeO_2 dispersion, band gap modification, and charge transport characteristics. The photocatalytic performance of the synthesized catalyst was evaluated toward the degradation of Reactive Blue 19 under UV and solar irradiation. A nonlinear fractional-order Langmuir–Hinshelwood kinetic model was employed to provide a more accurate interpretation of degradation behavior. In addition, catalyst stability and reusability were assessed to establish its potential application in real wastewater treatment. CeO_2/rGO photocatalysts are widely studied, but previous works mainly rely on simplified pseudo-first-order kinetics. Here, we demonstrate a novel approach by applying fractional-order LH kinetics to capture nonlinear photocatalytic behavior. This combined focus on material design and advanced kinetic modeling provides deeper mechanistic insight and a more realistic description compared to earlier CeO_2/rGO studies. This study demonstrates a sustainable synthetic route and provides new mechanistic insights into CeO_2/rGO photocatalysis using advanced kinetic analysis.

2 EXPERIMENTAL WORK

2.1 Materials

Analytical grade reagents including concentrated H_2SO_4, HCl, $KMnO_4$, $Ce(NO_3)_3 \cdot 6H_2O$, NaOH, ethanol (99.9%), and glycerol were procured and used without further purification. Fresh leaves of *Carica papaya* were collected locally and processed immediately to prepare the plant extract. Deionized water was used throughout the experiments. Reactive Blue 19 (Molecular Formula: $C_{22}H_{16}N_2Na_2O_{11}S_3$; Molecular Weight: 626.5 g/mol; λmax: 592 nm), an anionic anthraquinone dye, was selected as the model pollutant for photocatalytic studies.

2.2 Synthesis of Materials

2.2.1 Synthesis of Graphene Oxide

Graphene oxide (GO) was synthesized using a modified Hummers' method with controlled reaction conditions. Graphite powder (1 g) was added to chilled concentrated H_2SO_4 (23 mL) under continuous stirring while maintaining the temperature below 5 °C. $KMnO_4$ (3 g) was gradually introduced to prevent thermal runaway. The mixture was stirred for 1 hour and then allowed to reach room temperature. Subsequently, deionized water (46 mL) was added slowly, and the reaction was heated to 95 °C for 30 min. During the work-up, the pH of the suspension was carefully monitored and adjusted through repeated washing and filtration using 10% HCl and distilled water until a near-neutral pH (~6–7) was achieved. After dilution with 140 mL distilled water, the product was filtered and washed thoroughly to obtain purified GO. The formation of GO was visually confirmed by the characteristic color change from dark graphite to brownish-yellow dispersion, and the final yield was found to be ~85% based on the initial graphite used.

2.2.2 Preparation of Carica Papaya Leaf Extract

Fresh papaya leaves (25 g) were washed thoroughly, cut into small pieces, and ground into a paste. The paste was mixed with a 100 mL volume of deionized water and warmed at 60 °C filtered through Whatman No. 40 filter paper. The resulting extract was used immediately to avoid decomposition of biomolecules.

2.2.3 Green Reduction of GO to rGO

Graphene oxide (30 mg) was dispersed in 50 mL deionized water and ultrasonicated for 30 min. Papaya leaf extract (30 mL) was then added, and the mixture was refluxed at 95 °C for 12 hour in a round-bottom flask fitted with a condenser. The resulting black rGO was filtered, washed with water, and dried at 90 °C. The final

yield was found to be ~65% based on the initial graphite used.

2.2.4 Synthesis of CeO_2/rGO Nanohybrid

Cerium nitrate (250 mg) was dissolved in 150 mL glycerol and mixed with rGO (500 mg). The mixture was refluxed for 24 hours under a nitrogen atmosphere, promoting uniform nucleation of CeO_2 nanoparticles on the rGO sheets. After cooling, the solid product was separated, washed sequentially with water and ethanol, and dried at 100 °C.

2.3 Characterization Techniques

X-ray diffraction (XRD) was used to analyze crystallinity using a Cu–Kα radiation source (X' Pert Pro – PAnalytic). Surface morphology and nanoparticle dispersion were studied using SEM and HRTEM (JEOL-2100, Voltage 200 kV). Elemental composition was confirmed through EDX analysis. Raman spectroscopy was employed to evaluate disorder and defect density (LabRAM HR Evolution). UV–Vis diffuse reflectance spectroscopy (DRS - Perkin Elmer Model: Lambda 35) was used for optical band gap determination using Tauc analysis. Surface area and porosity were measured by BET analysis. UV–Vis spectrophotometry was used to monitor dye degradation by measuring absorbance at 592 nm.

2.4 Photocatalytic Degradation Experiments

Photocatalytic degradation of RB19 was conducted under UV and natural solar irradiation using annular photoreactor (Fig. 1). Dye solutions of known concentration were mixed with the required amount of catalyst and stirred in the dark for 30 min to establish adsorption–desorption equilibrium. UV-light irradiation experiments were conducted using an LED light source centered at ~395 nm with an average irradiance of 30 mW cm_{-2}, whereas photocatalytic experiments under natural sunlight were conducted between 11:00 and 14:00 IST in Namakkal (55F8+6CW, Namakkal, Tamil Nadu 637002, India) during the month of April under clear sky conditions. The average natural sunlight irradiance was measured to be 720 ± 30 W m^{-2} using a calibrated solar power meter. At regular intervals, aliquots were collected, centrifuged, and analyzed for residual dye concentration.

2.5 Kinetic Modeling

Photocatalytic degradation data were analyzed using the nonlinear fractional-order Langmuir–Hinshelwood (LH) kinetic model (Murti *et al*. 2025). Nonlinear fitting was carried out using least squares minimization to determine the reaction order (n) and apparent rate constant (k*app). This approach allowed minimization of concentration-based errors and provided a more accurate representation of heterogeneous photocatalysis compared to conventional linear models.

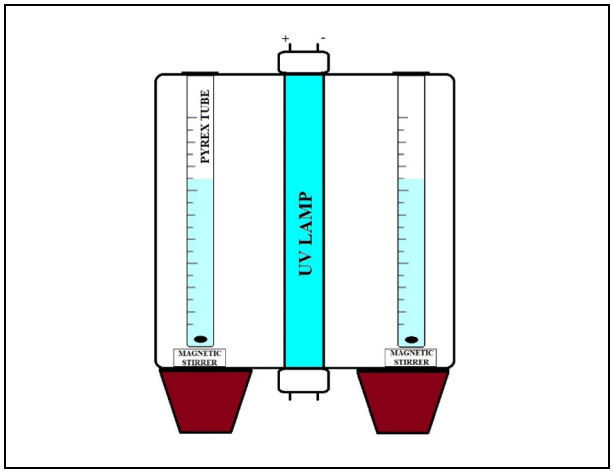


Fig. 1: Cross-sectional schematic of the annular photoreactor

3 RESULTS AND DISCUSSION

3.1 Structural and Morphological Characterization

The phase composition and crystallinity of the synthesized nanohybrid was examined by powder X-ray diffraction (XRD), as shown in Fig. 2(a). The diffraction peaks observed at 2θ values of 28.5°, 33.2°, 47.5°, 56.3°, and 76.8° correspond to the (111), (200), (220), (311), and (331) crystallographic planes of fluorite-structured CeO_2 (JCPDS No. 34-0394), confirming the formation of crystalline cerium oxide. In addition, a weak and broad diffraction peak centered around 2θ ≈ 19–22° was attributed to the disordered graphitic structure of graphene oxide (Siburian *et al.* 2018). Upon incorporation of CeO_2 nanoparticles onto GO sheets, the characteristic GO peak exhibited a noticeable reduction in intensity and broadening, indicating partial exfoliation and disruption of the layered graphitic structure. This attenuation of the GO diffraction peak further suggests strong interfacial interaction between CeO_2 nanoparticles and the GO support, confirming the successful anchoring of CeO_2 on the graphene-based platform. Peak broadening indicated nanoscale crystallite formation, consistent with TEM observations.

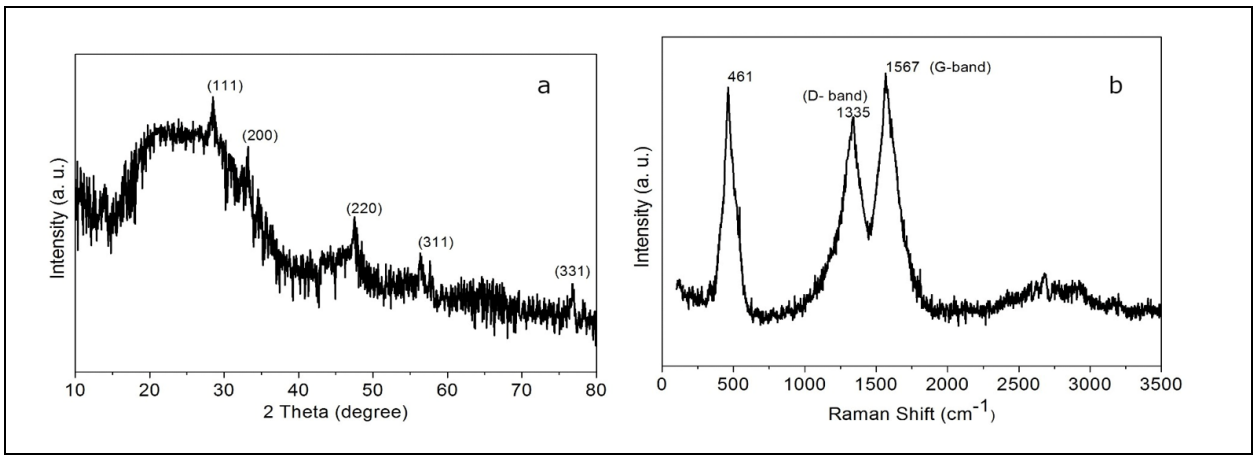


Fig. 2: (a) XRD pattern of CeO_2/rGO sample (b) The Raman spectrum of the CeO_2/rGO nanohybrid

The Raman spectrum of the CeO_2/rGO nanocomposite exhibits two prominent bands corresponding to the D band (~1335 cm^{-1}) and G band (~1567 cm^{-1}) of graphene-based materials (Fig 2(b)). Compared to GO, the G band of CeO_2/rGO shows a noticeable blue shift and significant band broadening, indicating restoration of sp^2 carbon domains and strong electronic interaction between CeO_2 nanoparticles and rGO sheets. The higher I_D/I_G intensity ratio further confirms the generation of defect sites and effective reduction of GO. In addition, a characteristic Raman active mode of fluorite CeO_2 was observed around 461 cm^{-1}, confirming the crystalline nature of CeO_2 in the nanocomposite. The observed Raman shifts and band broadening collectively suggest strong interfacial coupling, which facilitates efficient charge transfer during photocatalytic processes (Yuan *et al.* 2025).

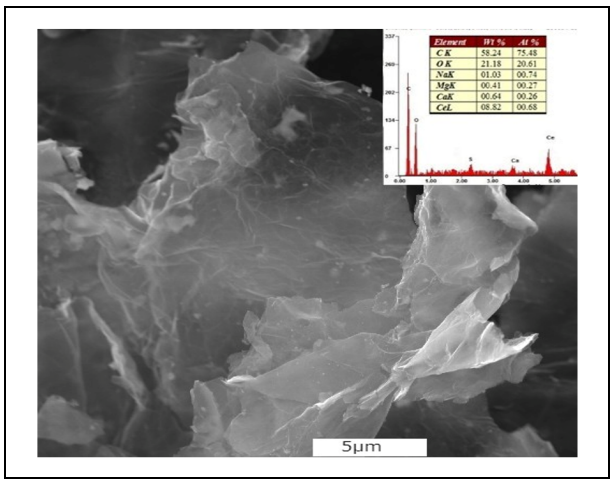


Fig. 3: SEM image of the CeO_2/rGO sample with the corresponding EDAX shown in the inset

The SEM image of the CeO_2/rGO composite shown in Fig. 3 indicates thin, wrinkled rGO sheets with CeO_2 nanoparticles uniformly dispersed and anchored on their surface, indicating good interaction between the oxide particles and the graphene support. The distribution of nanoparticles on the rGO sheets helps prevent agglomeration and provides a large surface area, enhancing the structural stability of the composite. The inset figure shows the corresponding EDAX spectrum, which confirms the presence of Ce, O, and C elements, verifying the successful formation of the CeO_2/rGO composite and indicating the absence of significant impurities.

The high-resolution transmission electron microscopy (HRTEM) image and selected area electron diffraction (SAED) study of the CeO_2/rGO nanocomposite (Fig. 4) provides direct evidence for the successful integration of CeO_2 nanoparticles onto the rGO matrix. Fig. 4(a) clearly reveals thin, wrinkled, and semi-transparent sheet-like structures corresponding to reduced graphene oxide, which serve as a supporting platform for the immobilization of CeO_2 nanoparticles. Dark contrast regions distributed over the rGO sheets are attributed to CeO_2 nanoparticles, indicating effective anchoring and minimal agglomeration. The nanoparticles exhibit nanoscale dimensions, consistent with the crystallite sizes estimated from XRD analysis.

The SAED pattern of the CeO_2/rGO nanocomposite further confirms its crystalline nature (Fig. 4(b)) (Veeresha *et al.* 2022). The SAED pattern exhibits a series of concentric diffraction rings rather than discrete spots, indicating the polycrystalline nature of the CeO_2 nanoparticles uniformly distributed on the rGO sheets. The prominent diffraction rings can be indexed to the (111), (200), (220), and (311) planes of cubic fluorite CeO_2, which is in good agreement with the XRD results (Deori *et al.* 2013). The absence of additional diffraction rings corresponding to impurity phases confirms the high phase purity of the synthesized nanocomposite. Moreover, the diffused background intensity observed in the SAED pattern is attributed to the amorphous or turbostratic structure of rGO. The coexistence of sharp CeO_2 diffraction rings and the diffuse rGO background suggests strong interfacial contact between crystalline CeO_2 nanoparticles and the graphene-based support, which is beneficial for efficient charge transfer during photocatalytic processes.

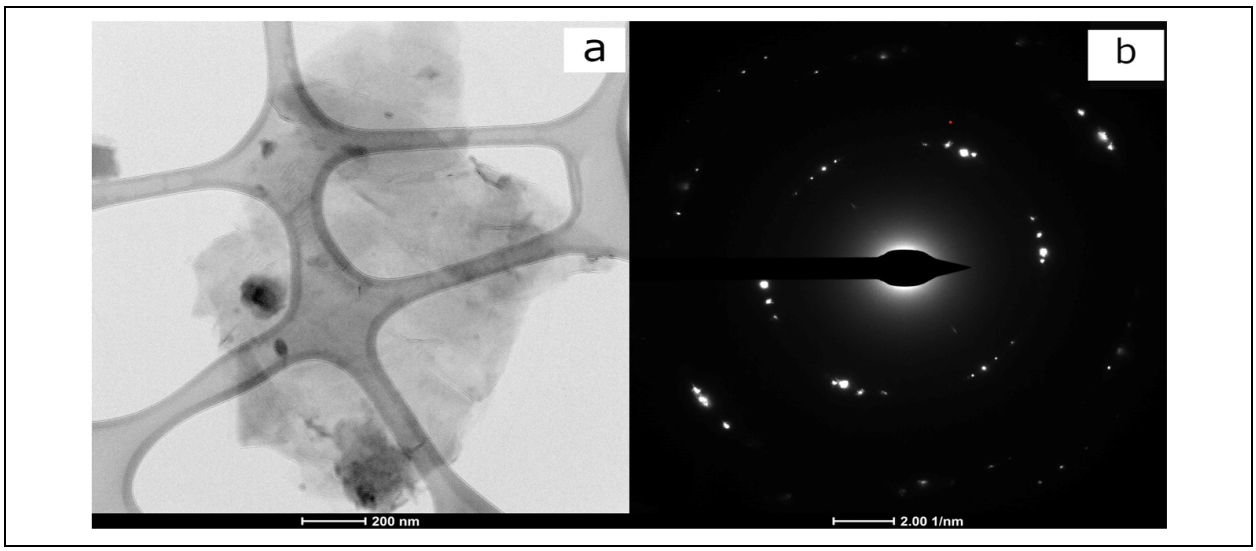


Fig.4: (a) HRTEM micrographs and (b) SAED of CeO_2/rGO nanohybrid

The BET analysis revealed a specific surface area of 95 m^2/g for the CeO_2/rGO nanohybrid, significantly higher than pristine CeO_2 (Majani *et al.* 2025). The pore diameter, and pore volume were found to be 8.6 nm, and 0.27 cm^3/g, respectively. The increased surface area and porous structure enhance dye adsorption and photocatalytic performance.

The optical properties of the synthesized sample were investigated using UV–visible diffuse reflectance spectroscopy (Graph not included). The optical band gap energy (E_g) was estimated from the absorption edge using the relation E_g (eV) = 1239.8/λ, where 1239.8 is a constant derived from the product of Planck's constant and the velocity of light, and λ represents the wavelength of the absorbed light expressed in nm. The photocatalytic experiments were performed using ~395 nm LED light source (~3.14 eV), which provides photon energy higher than the estimated band gap (2.91 eV, corresponding to 426 nm), ensuring effective photoexcitation of the catalyst. In addition, the band gap was evaluated using Tauc analysis, assuming an indirect allowed transition, which is typical for CeO_2-based materials. The Tauc plot was constructed by plotting $(\alpha h\nu)^{1/2}$ versus photon energy (hν), and the extrapolation of the linear region to the energy axis further confirmed the band gap value (graph not included). The reduced band gap indicates enhanced visible light absorption, which is beneficial for photocatalytic applications (Chen *et al.* 2024a).

3.2 Photocatalytic Degradation of RB19 Dye

3.2.1 Influence of Catalyst Dosage

The influence of catalyst dosage on dye degradation was systematically examined by varying the amount of catalyst from 10 to 60 mg (Fig. 5(a)). An increase in photocatalytic efficiency was observed with increasing catalyst dosage up to 50 mg, which can be attributed to the availability of a greater number of active surface sites and enhanced generation of reactive species such as hydroxyl and superoxide radicals. The increased catalyst loading also improves light absorption by providing a larger surface area for photon–catalyst interaction. However, beyond the optimum dosage of 50 mg, a decline in degradation efficiency was observed. This reduction can be explained by excessive light scattering and shielding effects caused by higher catalyst concentrations, which limit the penetration of light into the reaction medium. In addition, increased particle agglomeration at higher loadings reduces the effective surface area and restricts the accessibility of active sites. Consequently, the reduced photon utilization and mass transfer limitations outweigh the benefits of increased catalyst amount, leading to a decrease in photocatalytic performance (Ballari *et al.* 2008).

3.2.2 Effect of Initial pH

The photocatalytic degradation of RB19 was strongly influenced by the pH of the dye solution under both UV and solar irradiation (Khan *et al.* 2015). As shown in Fig. 5(b), the degradation efficiency increased from pH 2 to reach a maximum in the mildly acidic range (pH 4–5), followed by a gradual decline at higher pH values. This trend was consistently observed under both irradiation conditions, with UV light showing higher degradation efficiency than solar light.

The enhanced degradation observed at mildly acidic pH can be primarily attributed to favorable electrostatic interactions between the photocatalyst surface and the anionic RB19 dye molecules (Mahmoodi *et al.* 2011). At lower pH values, the catalyst surface becomes positively charged due to protonation, which promotes strong adsorption of the negatively charged dye molecules onto the catalyst surface. This improved adsorption facilitates effective interaction between the

dye molecules and photogenerated reactive species, thereby enhancing degradation. However, at very low pH (pH 2–3), excess protons can act as scavengers for photogenerated electrons, suppressing the formation of hydroxyl radicals and limiting the overall photocatalytic efficiency.

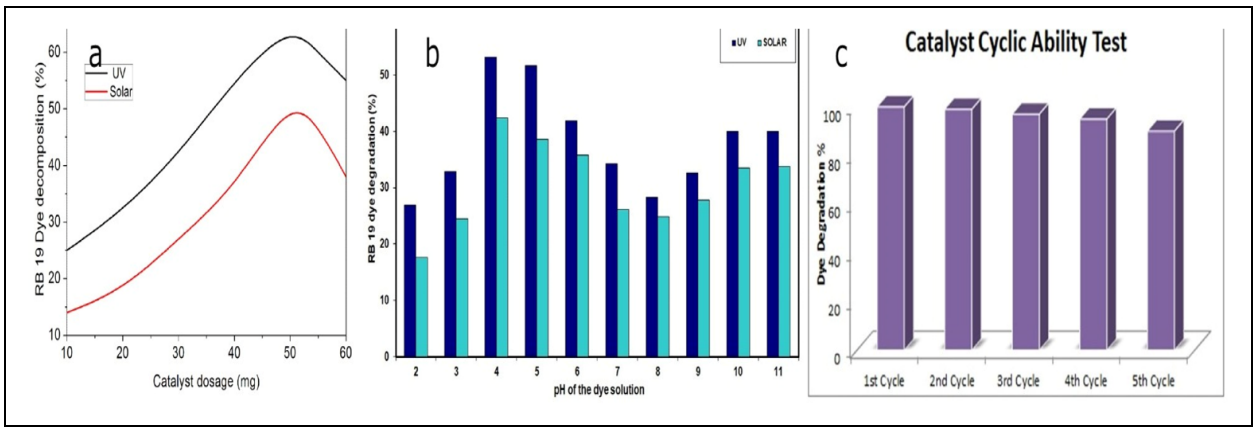


Fig. 5: (a) Effect of catalyst dosage on photocatalytic degradation of RB19 dye (b) effect of pH on photocatalytic degradation of RB19 dye and (c) recycling experiment of the CeO_2/rGO nanohybrid

At pH values above 6, the degradation efficiency decreases due to electrostatic repulsion between the negatively charged catalyst surface and the anionic RB19 molecules, which reduces dye adsorption. In addition, excessive hydroxyl ions present under alkaline conditions can lead to increased recombination of photogenerated electron–hole pairs and scavenging of hydroxyl radicals, thereby decreasing the availability of reactive oxygen species for dye degradation. Furthermore, higher pH conditions may increase solution turbidity, resulting in reduced light penetration and lower photon utilization (Chen *et al.* 2024b).

The consistently higher degradation efficiency observed under UV irradiation compared to solar irradiation is due to the higher photon energy and intensity of UV light, which enhances charge carrier generation and accelerates photocatalytic reactions (Nagaraja *et al.* 2012).

Zeta potential measurements of the CeO_2–rGO photocatalyst and RB19 were carried out at different pH values using a dynamic light scattering analyzer. The results confirmed that the catalyst surface is slightly positive to near-neutral at pH 4–5 (approximately +5 to +15 mV) and becomes increasingly negative (−20 to −40 mV) at higher pH, while RB19 remains negatively charged across the studied range (−20 to −55 mV) due to the presence of sulfonate ($–SO_3^-$) groups. This pH-dependent surface charge behavior, influenced by the near-neutral point of zero charge of CeO_2 and negatively charged functional groups of rGO, promotes strong electrostatic attraction at acidic pH and repulsion under alkaline conditions. These findings experimentally validate the proposed electrostatic interaction mechanism and explain the observed pH-dependent photocatalytic degradation efficiency.

3.2.3 Kinetic Analysis using Fractional-Order LH Model

The photocatalytic degradation kinetics of RB19 dye over the CeO_2/rGO nanohybrid were systematically analyzed using the Langmuir–Hinshelwood kinetic model, which is widely accepted for heterogeneous photocatalytic systems (Murti *et al.* 2025). The experimental data showed appreciable linearity with the pseudo-first-order kinetic model, as evidenced by higher R^2 values compared to second-order plots. Though the pseudo-first-order kinetics provided a reasonable fit, but failed to capture deviations caused by dye intermediates and heterogeneous surface behavior (Jadaa *et al.* 2021; Chu *et al.* 2025). The nonlinear fractional-order LH model produced superior fitting accuracy with reaction orders ranging from 0.38–0.58 (UV) and 0.30–0.48 (solar) (Xu *et al.* 2020). The fractional reaction order between 0 and 1 for both UV and solar irradiation provided a more accurate description of the catalyst substrate system (Ollis, 2018). This fractional-order behavior reflects the combined influence of adsorption equilibrium and surface reaction kinetics inherent to heterogeneous photocatalysis. The non-linear fitting approach minimized concentration-based errors more effectively than linearized models, confirming that the photodegradation of RB19 over CeO_2/rGO follows fractional-order LH kinetics, consistent with previously reported photocatalytic dye degradation systems (Wang, 2018). This confirmed the complex nature of RB19 degradation involving competitive adsorption and intermediate formation.

The apparent rate constant (k_{app}), obtained from the linear plots of $\ln(C_t/C_o)$ versus time (graph not shown), revealed a gradual decrease with increasing dye concentration, suggesting partial occupation of active sites and the onset of adsorption-controlled kinetics. The

relationship between initial dye concentration (C_o) and initial reaction rate (r_o) followed a near-linear trend at lower concentrations without reaching saturation, confirming that complete surface coverage of the catalyst was not attained within the investigated concentration range.

3.2.4 Photocatalytic Mechanism

Under illumination, CeO_2 generates electron–hole pairs. The rGO matrix facilitates rapid electron transport, suppressing recombination and enhancing radical formation (Pu *et al.* 2017). Transferred electrons reduce dissolved oxygen to $O_2^{\bullet-}$ radicals, while holes oxidize surface OH^- to •OH radicals. These reactive oxygen species attack RB19 dye molecules, leading to progressive decomposition.

3.2.5 Catalyst Stability and Reusability

Recycling experiments demonstrated that the CeO_2/rGO nanohybrid retained more than 95% of its degradation efficiency after four consecutive cycles (Fig. 5(c)). The strong anchoring of CeO_2 nanoparticles on rGO contributed to its structural stability and resistance to photocorrosion (Verma *et al.* 2016).

3.2.5 Comparative Literature of CeO_2–based Photocatalysts for Dye Degradation

Table 1. Comparative review of CeO_2-based photocatalysts in dye degradation studies

Material Composition	Synthesis Method	Pollutant	Degradation (%)	Time (min)	Key Findings	Reference
CeO_2–V_2O_5/rGO	Hydrothermal method	Cefotaxime (CTX)	99% (visible light); 88.1% (sunlight)	150 (visible); 250 (sunlight)	enhanced visible-light photocatalysis; pseudo-first-order kinetics (k = 0.03–0.06 min^{-1}); good stability and reusability.	(Tran *et al.* 2024)
Ag-doped CeO_2 nanorods/rGO (Ag@CeO_2/rGO)	Green synthesis using *Punica granatum* peel extract	Methylene Blue (MB), 4-Nitrophenol (4-NP)	100% (MB)	60	enhanced photocurrent density (215 mA cm^{-2}).	(Vanasundari *et al.* 2024)
CeO_2 nanoparticles/rGO	Green hydrothermal + calcination (in-situ growth)	Rhodamine B, Methyl Orange	94.7% (RhB)	120	CeO_2 nanoparticles uniformly dispersed on rGO; stable after 5 cycles (87.2%).	(Sun *et al.* 2023)
CeO_2@rGO	Chemical synthesis (nanoceria decorated on rGO)	Methylene Blue (MB), Congo Red (CR)	92% (MB); 83% (CR)	300	hydrogel composite (CeO_2@rGO-TG) enabled easy recovery and reuse of catalyst.	(Garg *et al.* 2020)
rGO/CeO_2	Solution combustion (Ashwagandha plant + tartaric acid fuel) followed by reflux	Rose Bengal (RB)	~95%	180	Green synthesis; first-order kinetics; half-life 40.96 min; stable up to five cycles;	(Roopa *et al.* 2024a)
CeO_2/rGO	Green combustion (lemongrass fuel) + reflux method	Methyl Violet (MV)	~99%	Not specified	High photocatalytic efficiency with rate constant 0.03971 min^{-1}; reactive species and TOC removal studied; good catalyst reusability.	(Roopa *et al.* 2024b)
rGO–CeO_2 nanocomposite	Co-precipitation method	Methylene Blue (MB)	94.92%	80	High degradation under UV light (254 nm); pseudo-second-order kinetics; strong adsorption and stable up to four cycles.	(Rahman *et al.* 2025)
CeO_2–rGO (green synthesis)	Plant extract mediated	Reactive Blue 19	High (>95)	Shorter	Green synthesis, 4–8 nm particles, fractional LH kinetics, >95% reuse stability	Present work

4. CONCLUSIONS

A green and sustainable approach was successfully developed for synthesizing a CeO_2–doped reduced graphene oxide (CeO_2/rGO) nanohybrid using *Carica papaya* leaf extract as a natural reducing agent. Structural and morphological characterization confirmed the uniform anchoring of 4–8 nm CeO_s nanoparticles on rGO sheets, along with significant improvements in surface area, crystallinity, and optical properties. The reduced band gap (2.91 eV) and enhanced charge-transfer characteristics enabled superior photocatalytic activity toward the degradation of Reactive Blue 19 under both UV and solar irradiation. The nonlinear fractional-order Langmuir–Hinshelwood kinetic model provided a more accurate representation of the degradation process compared to conventional linearized models, revealing fractional reaction orders (0.30–0.58) characteristic of heterogeneous photocatalysis. The nanohybrid displayed excellent stability and retained over 95% activity after four reuse cycles, demonstrating strong potential for real wastewater treatment applications. Future work may focus on mechanistic validation using radical scavenging, mineralization studies, and scaling the process for real effluent treatment.

FUNDING

This research received no specific grant from any funding agency in the public, commercial, or not-for-profit sectors.

CONFLICTS OF INTEREST

The authors declare that there is no conflict of interest.

COPYRIGHT

This article is an open-access article distributed under the terms and conditions of the Creative Commons Attribution (CC BY) license (http://creativecommons.org/licenses/by/4.0/).

REFERENCES

Ahamed, M., Ali, S. M., Lateef, R., Dotto, G. L. and Hisham, A. A., Oxygen-Vacancy Engineering and Junction Design in CeO_2 Nanomaterials for Photocatalysis and Antibacterial Action: A Review, *Res. Eng.,* 28:108076 (2025). https://doi.org/10.1016/j.rineng.2025.108076

Ansari, A., Azzahra, G., Fairuz, N. G., Momin, M. M. and Abu, A. A. T., Oxides and Metal Oxide/Carbon Hybrid Materials for Efficient Photocatalytic Organic Pollutant Removal, *Catal.,* 15(2), 134 (2025). https://doi.org/10.3390/catal15020134

Ballari, M. D. L. M., Brandi, R., Alfano, O. and Alberto, C., Mass Transfer Limitations in Photocatalytic Reactors Employing Titanium Dioxide Suspensions, *Chem. Eng. J.,* 136(1), 50–65 (2008). https://doi.org/10.1016/j.cej.2007.03.028

Chen, J., Chen, Y., Shuai, J., Chen, X., Zhang, D., Xi, L., Fang, X., Zou, F. and Wei, F., Enhancement of Visible Light Adsorption and Photocatalytic Degradation Activity of Organic Dye by Coating Semiconducting TiO_2 Shell on Plasmonic Au Particles, *J. Alloys Compd.,* 1009, 176938 (2024a). https://doi.org/10.1016/j.jallcom.2024.176938

Chen, Y., Ma, D., He, G. and Pan, S., Effects of pH on the Photocatalytic Activity and Degradation Mechanism of Rhodamine B over Fusiform Bi Photocatalysts under Visible Light, *Water,* 16(17), 2389 (2024b). https://doi.org/10.3390/w16172389

Chu, K. H., Bollinger, J. C. and Jakub, K., Pseudo-First-Order Kinetics in Environmental Adsorption: Why Are There Two Distinct Equations? *Environ. Surf. Interf.,* 3, 191–195 (2025). https://doi.org/10.1016/j.esi.2025.07.001

Deori, K., Gupta, D., Saha, B., Awasthi, S. K. and Deka, S., Introducing Nanocrystalline CeO_2 as Heterogeneous Environmental Friendly Catalyst for the Aerobic Oxidation of Para-Xylene to Terephthalic Acid in Water, *J. Mater. Chem. A,* 1(24), 7091 (2013). https://doi.org/10.1039/c3ta01590d

El Mchaouri, M., Safiya, M., Dikra, A., Wafaa, B., Rachid, E., Essadki, A., Barka, N. and Elhalil, A., Engineering TiO_2 Photocatalysts for Enhanced Visible-Light Activity in Wastewater Treatment Applications, *Tetrahedron Green Chem.,* 6, 100084 (2025). https://doi.org/10.1016/j.tgchem.2025.100084

Garg, D., Matai, I., Garg, A. and Sachdev, A., Tragacanth Hydrogel Integrated CeO_2 @rGO Nanocomposite as Reusable Photocatalysts for Organic Dye Degradation, *Chem. Select,* 5(34), 10663–10672 (2020). https://doi.org/10.1002/slct.202002041

Jadaa, W., Anand, P. and Ray, A. K., Photocatalytic Degradation of Diazo Dye over Suspended and Immobilized TiO_2 Catalyst in Swirl Flow Reactor: Kinetic Modeling, *Processes,* 9(10), 1741 (2021). https://doi.org/10.3390/pr9101741

Khan, M. A. N., Maria, S., Fazli, W. and Khan, R., Removal of Reactive Blue 19 Dye by Sono, Photo and Sonophotocatalytic Oxidation Using Visible Light, *Ultrason. Sonochem.* 26, 370–377 (2015). https://doi.org/10.1016/j.ultsonch.2015.04.012

Kumar, M., Singh, V. P., Bhat, S. B. and Raj, K., Environmental Risks of Textile Dyes and Photocatalytic Materials for Sustainable Treatment: Current Status and Future Directions, *Discover Environ.,* 3(1), 132 (2025). https://doi.org/10.1007/s44274-025-00337-0

Mahmoodi, N. M., Arami, M., Hajir, B. and Shooka, K., The Effect of pH on the Removal of Anionic Dyes from Colored Textile Wastewater Using a Biosorbent, *J. Appl. Polym. Sci.,* 120(5), 2996–3003 (2011). https://doi.org/10.1002/app.33406

Majani, S. S., Singh, P., Kumari, P., Setty, P. B. S., Chandan, S., Srinivasa, C., Abass, K. S., Iqbal, M., Amachawadi, R. G., Stupin, V., Silina, E. and Kollur, S. P., Cerium Oxide Nanoparticles Prepared through Bio-Combustion Using Ficus Carica as Effective Antioxidant, Anticancer and Dye Degrading Agent, *Sci. Rep.,* 15(1), 30285 (2025). https://doi.org/10.1038/s41598-025-13914-3

Mondal, A., Aarya, P., Gupta, S. and Ravi, S. V., Boosting Photocatalytic Activity Using Reduced Graphene Oxide (RGO)/Semiconductor Nanocomposites: Issues and Future Scope, *ACS Omega,* 6(13), 8734–8743 (2021). https://doi.org/10.1021/acsomega.0c06045

Murti, R. H. A., Jawwad, M. A. S., Khusnul, A. K. and Nurul, E. H., High Efficiency on Resin Photocatalysis: Study on Application and Kinetic Mechanism Using Langmuir Hinshelwood Model, *S. Afr. J. Chem. Eng.,* 53, 87–95 (2025). https://doi.org/10.1016/j.sajce.2025.04.013

Nagaraja, R., Nagaraju, K., Girija, C. R. and Nagabhushana, B. M., Photocatalytic Degradation of Rhodamine B Dye under UV/Solar Light Using ZnO Nanopowder Synthesized by Solution Combustion Route, *Powder Technol.,* 215–216, 91–97 (2012). https://doi.org/10.1016/j.powtec.2011.09.014

Ollis, D. F., Kinetics of Photocatalyzed Reactions: Five Lessons Learned, *Front. Chem.,* 6, 378 (2018). https://doi.org/10.3389/fchem.2018.00378

Pu, Y. C., Chou, H. Y., Kuo, W. S. and Hsu, K. H., Interfacial Charge Carrier Dynamics of Cuprous Oxide-Reduced Graphene Oxide (Cu_2O-rGO) Nanoheterostructures and Their Related Visible-Light-Driven Photocatalysis, *Appl. Catal. B-Environ*., 204, 21–32 (2017). https://doi.org/10.1016/j.apcatb.2016.11.012

Rahman, A., Naime, J., Habib, M. A., Imran, A. S., Mahiuddin, M. and Rezaul, K. K. M., Reduced Graphene Oxide – CeO_2 Nanocomposites for Photocatalytic Dye Degradation, *Mater. Chem. Phys.* 332, 130210 (2025). https://doi.org/10.1016/j.matchemphys.2024.130210

Roopa, M. C., Thirumala, S., Kallimani, S. and Manohara, B. M., Green and Reflux Method Synthesis of CeO_2/rGO for Their Characterization and Photodegradation of Dye, *Sustain. Chem. One World,* 4, 100024(2024a). https://doi.org/10.1016/j.scowo.2024.100024

Roopa, M. C., Thirumala, S., Kallimani, S. and Manohara, B. M., Green Synthesis and Characterization of Nano Reduced Graphene Oxide/Cerium Oxide (rGO/CeO_2) for Rose Bengal Dye Degradation, *J. Alloys Compd.,* 4, 100033 (2024b). https://doi.org/10.1016/j.jacomc.2024.100033

Sahu, S. K., Palai, A. and Sahu, D., Photocatalytic Applications of Metal Oxide-Based Nanocomposites for Sustainable Environmental Remediation, *Sustainable Chem. Environ.,* 8, 100162 (2024). https://doi.org/10.1016/j.scenv.2024.100162

Siburian, R., Sihotang, H., Lumban, R. S., Supeno, M. and Simanjuntak, C., New Route to Synthesize of Graphene Nano Sheets, *Orient. J. Chem.,* 34(1), 182–87 (2018). https://doi.org/10.13005/ojc/340120

Sun, B., Chen, W., Zheng, W., Zhang, H., Liu, T. X., Elmarakbi, A. and Fu, Y., In-Situ Controlled Growth of Ultrafine CeO_2 Nanoparticles on Reduced Graphene Oxides for Efficient Photocatalytic Degradation, *J. Catal.,* 424, 106–120 (2023). https://doi.org/10.1016/j.jcat.2023.05.014

Tran, D. T., Ha, T. H., Vu, T. P. T., Nguyen, V. N. and Pham, T. D., Novel CeO_2-V_2O_5/rGO Tertiary Photocatalyst for Improved Cefotaxime Degradation Using Visible-Light, *Inorg. Chem. Commun.,* 161, 112044 (2024). https://doi.org/10.1016/j.inoche.2024.112044

Vanasundari, K., Ponnarasi, P. and Mahalakshmi, G., A Green Approach to Synthesis of Ag-Doped CeO_2 Nanorods Embedded Reduced Graphene Oxide Nanocomposite for Excellent Photocatalytic and Antimicrobial Activity, *Inorg. Chem. Commun*., 165, 112523 (2024). https://doi.org/10.1016/j.inoche.2024.112523

Veeresha, G., Krishnamurthy, G. and Shivakumar, M. S., Cobalt Nanocrystals Doped on CeO_2/RGO Nanocomposite for Supercapacitor Applications, *Inorg. Chem. Commun.,* 138, 109232 (2022). https://doi.org/10.1016/j.inoche.2022.109232

Verma, R. and Samdarshi, S. K., In Situ Decorated Optimized CeO_2 on Reduced Graphene Oxide with Enhanced Adsorptivity and Visible Light Photocatalytic Stability and Reusability, *J. Phys. Chem. C.,* 120(39), 22281–22290 (2016). https://doi.org/10.1021/acs.jpcc.6b04493

Villagrán, Z., Anaya, E. L. M., Carlos, A. V. C., Jara, S. J. M., Martin, J. G. R., Edward, F. A. V., Ernesto, R. L., Noe, R. B., Ivan, B. L. and Fernando, M. E., Plant-Based Extracts as Reducing, Capping, and Stabilizing Agents for the Green Synthesis of Inorganic Nanoparticles, *Resources,* 13(6), 70 (2024). https://doi.org/10.3390/resources13060070

Wang, C. L., Fractional Kinetics of Photocatalytic Degradation, *J. Adv. Dielectr.,* 08(05), 1850034 (2018). https://doi.org/10.1142/S2010135X18500340

Wu, M., Shu, Z., Huang, X., Chen, Z. and Zhi, D., Insight into the Coupled Processes of Electro-Oxidation and Other Techniques for Organic Removal from Water and Wastewater, *Desalin. Water Treat.,* 324, 101458 (2025). https://doi.org/10.1016/j.dwt.2025.101458

Xu, Q., Björn, E., Mansour, S. and Kezhen, Y., A New Nonlinear Viscoelastic Model and Mathematical Solution of Solids for Improving Prediction Accuracy, *Sci. Rep.,* 10(1), 2202 (2020). https://doi.org/10.1038/s41598-020-58240-y

Yuan, R., Yiwen, G., Illke, G., Nahian, S., Li, Y. S., Jang, S., Noh, G. A. and Kim, S. H., Raman Spectroscopy Analysis of Disordered and Amorphous Carbon Materials: A Review of Empirical Correlations, *Carbon,* 238, 120214 (2025). https://doi.org/10.1016/j.carbon.2025.120214